

# Biosorption of azo dyes by raspberry-like $\text{Fe}_3\text{O}_4$ @yeast magnetic microspheres and their efficient regeneration using heterogeneous Fenton-like catalytic processes over an up-flow packed reactor

Rui Song<sup>1</sup> · Bo Bai<sup>2</sup> · Gianluca Li Puma<sup>3</sup> ·  
Honglun Wang<sup>2</sup> · Yourui Suo<sup>2</sup>

Received: 4 December 2014 / Accepted: 12 March 2015 / Published online: 21 March 2015  
© Akadémiai Kiadó, Budapest, Hungary 2015

**Abstract** Raspberry-like  $\text{Fe}_3\text{O}_4$ @yeast composite microspheres, whose properties integrate the biosorption features of yeast cells with the excellent magnetic and catalytic properties of  $\text{Fe}_3\text{O}_4$  nanoparticles, were synthesized by a simple electrostatic-interaction-driven self-assembly heterocoagulation. They were successfully applied in an up-flow packed column for the removal of the model water contaminant methylene blue dye (MB) by consecutive bioadsorption-heterogeneous Fenton oxidation cycles. The as-synthesized  $\text{Fe}_3\text{O}_4$ @yeast composites were characterized by field emission scanning electron microscopy, energy-dispersive spectroscopy (EDS), powder X-ray diffraction and Fourier transform infrared spectroscopy. The adsorption process was controlled by the electrostatic interactions between the adsorbent and contaminant. The adsorbent is suitable for the adsorption of positively charged compounds at mildly acidic pH, neutral and alkaline pH, with the highest performance observed at alkaline pH. The experimental breakthrough curves measured at different influent MB concentration, flow rate, bed height and pH were modeled by the Yoon-Nelson model. The in situ regeneration of the contaminant-loaded  $\text{Fe}_3\text{O}_4$ @yeast microspheres and their reuse in multiple cycles was demonstrated by triggering the heterogeneous Fenton-like reaction catalyzed by

**Electronic supplementary material** The online version of this article (doi:[10.1007/s11144-015-0854-z](https://doi.org/10.1007/s11144-015-0854-z)) contains supplementary material, which is available to authorized users.

✉ Bo Bai  
baibochina@163.com; baibo@chd.edu.cn

<sup>1</sup> College of Environmental Science and Engineering, Chang'an University, Xi'an 710054, People's Republic of China

<sup>2</sup> Northwest Plateau Institute of Biology, Chinese Academy of Sciences, Xining 810001, People's Republic of China

<sup>3</sup> Environmental Nanocatalysis and Photoreaction Engineering, Department of Chemical Engineering, Loughborough University, Loughborough LE11 3TU, UK

the supported magnetite. The raspberry-like  $\text{Fe}_3\text{O}_4$ @yeast magnetic microsphere should be a promising and practical adsorbent for removal and destruction of positively charged organic compounds in wastewater.

**Keywords** Yeast · Iron oxide · Fixed-bed · Fenton-like reaction · Regeneration · Wastewater

## Introduction

Organic azo dyes represent more than half of all coloring compounds used by the world textile industry. It has been estimated that 15 % of this is released into the environment without an appropriate treatment [1]. Organic azo dyes in wastewater have been classified as priority pollutants particularly owing to the toxicity of their microbial metabolites, which can be mutagenic, genotoxic and carcinogenic [2]. Traditional physico-chemical treatment techniques such as absorption, oxidization, and flotation are usually ineffective to treat low azo dyes concentrations [3]. Biological materials such as microorganisms (including bacteria, fungi, and algae) [4] and biomass can remove a broad range of azo dyes [5, 6]. However, an efficient and sustainable method for pollution abatement that uses biosorbents requires the regeneration and reuse of the sorbent, the destruction of the sorbed/desorbed pollutants, and the safe disposal of the sorbent to the environment. Yeast is an effective biosorbent [7] which meets several green requirements for large-scale pollutant removal including, high selectivity, efficiency, cost-effectiveness, availability and biocompatibility.

Heterogeneous Fenton processes are powerful methods for the destruction of azo dyes in aqueous solutions [8–10], especially, those catalyzed by nanosized magnetite ( $\text{Fe}_3\text{O}_4$ ) particles [11–13]. In this system, the octahedral site of the magnetite structure can easily accommodate both  $\text{Fe}^{2+}$  and  $\text{Fe}^{3+}$ , allowing the Fe species to be reversibly oxidized and reduced producing  $\cdot\text{OH}$  radicals when in the presence of  $\text{H}_2\text{O}_2$  [14, 15]. Furthermore,  $\text{Fe}_3\text{O}_4$  nanoparticles can be easily separated from the reaction system by a simple magnetic separation procedure.

The treatment of contaminated streams by Fenton oxidation with slurry suspensions of  $\text{Fe}_3\text{O}_4$  can be inefficient since uses it large volumes of reagents/catalyst, the water matrix can inefficiently consume  $\cdot\text{OH}$  radicals and large contact times are often required. In contrast, the efficiency of the heterogeneous Fenton process for the treatment of wastewater can be increased significantly by applying an enrichment or pre-concentration sorption method prior to the oxidation of the contaminants by the Fenton process on immobilized magnetite.

The combination of an inorganic catalyst with a biological sorbent into hybrid or composite material is attracting increasing attention as it enables new functional properties, which are not possible in their starting components. For example, a new class of complex nano-structured hybrid microspheres with a raspberry-like structure can provide a unique micro/nano-environment which has found new applications in the material, chemical, medical and environmental sectors [16–20]. Bai et al. have synthesized novel raspberry-like  $\text{TiO}_2$ @yeast composites, which were effective

photocatalysts for the degradation of dyes [21]. The raspberry shape provided larger surface area of the supported catalyst. However, such materials required the use of UV light photons, which restrict their technological development.

In this study, we investigate a new composite material, made of raspberry-like  $\text{Fe}_3\text{O}_4$ @yeast microspheres that integrate the biosorption features of yeast cells with the excellent magnetic and catalytic properties of  $\text{Fe}_3\text{O}_4$  nanoparticles, and its application for the effective removal of contaminants from wastewater by consecutive biosorption and heterogeneous Fenton oxidation/regeneration cycles. In this new material, the traditional magnetic  $\text{Fe}_3\text{O}_4$  nano-particles were anchored on the yeast surface by an electrostatic self-assembly process that produced a heterogeneous Fenton catalyst with a unique raspberry-like microstructure. The effectiveness of the raspberry-like  $\text{Fe}_3\text{O}_4$ @yeast composite microspheres for the removal of the cationic dye methylene blue (MB), a model compound used in the standardization of degradation experiments (e.g., ISO 10678:2010), was investigated in a continuous, up-flow, fixed-bed column system. The modeling of the adsorption phenomena and breakthrough profiles allowed the prediction of the breakthrough time after which the in situ regeneration of the composite material and the decomposition of MB was triggered through the heterogeneous Fenton reaction catalyzed by the  $\text{Fe}_3\text{O}_4$  nanoparticles. The robustness of the composite catalytic biosorbent was assessed for multiple adsorption/regeneration cycles.

## Materials and methods

### Materials

All chemicals used were of analytical grade and used without further purification. The powdered yeast was purchased from Angel Yeast Company. Ferric chloride hexahydrate ( $\text{FeCl}_3 \cdot 6\text{H}_2\text{O}$ ), absolute ethanol (95 wt%), formaldehyde ( $\text{CH}_2\text{O}$ ), hydrazine hydrate ( $\text{N}_2\text{H}_4 \cdot \text{H}_2\text{O}$ ), methylene blue (MB), and sulfuric acid ( $\text{H}_2\text{SO}_4$ ) were provided by Xi'an Chemical Agent Corp. Doubly deionized water was used throughout all the experiments.

### Preparation of $\text{Fe}_3\text{O}_4$ @yeast composite microspheres

$\text{Fe}_3\text{O}_4$  nanoparticles were first synthesized through a hydrothermal method using  $\text{FeCl}_3 \cdot 6\text{H}_2\text{O}$  as a single iron source. Briefly,  $\text{FeCl}_3 \cdot 6\text{H}_2\text{O}$  (1.20 g),  $\text{CH}_2\text{O}$  (2 mL) and  $\text{N}_2\text{H}_4 \cdot \text{H}_2\text{O}$  (5 mL) were dissolved in deionized water (40 mL) under magnetic stirring for 15 min. The solution was then transferred to a Teflon-lined stainless-steel autoclave and heated at 120 °C. After 5 h of reaction, the autoclave was cooled to room temperature. The black  $\text{Fe}_3\text{O}_4$  nanoparticles were collected magnetically and washed with three consecutive cycles of ethanol and distilled water and then dried in vacuum at 80 °C for 1 h. The dried  $\text{Fe}_3\text{O}_4$  nanoparticles were then re-dispersed in 150 mL of distilled water and the pH adjusted to 5 by adding  $\text{H}_2\text{SO}_4$  (1 M). The suspension was stirred for 30 min to promote the de-aggregation of the  $\text{Fe}_3\text{O}_4$  nanoparticles. In a separate vessel, 1000 g of yeast powder was washed with

distilled water and ethanol three times. It was dispersed in 150 mL of distilled water and the pH was adjusted to 5 by adding  $\text{H}_2\text{SO}_4$  (1 M). The suspension was magnetically stirred for 30 min to facilitate the dispersion of the yeast particles. Finally, the suspensions of  $\text{Fe}_3\text{O}_4$  nanoparticles and yeast were blended, under continuous stirring for 1 h at room temperature, and then the suspension was left for 3 h without further stirring, during which raspberry-like  $\text{Fe}_3\text{O}_4$ @yeast microspheres were produced via electrostatic self-assembly. The products were collected with a magnet, washed with distilled water and ethanol three times, and then dried at 80 °C for further use.

### Material characterization

The particle size and surface morphology of the samples were observed by a Philips XL 30 field emission scanning electron microscope (FE-SEM). The elemental composition of the composite microspheres was determined with the energy-dispersive spectroscopy (EDS) of the FE-SEM. The crystallographic structures of the samples were identified by powder X-ray diffraction (XRD) using  $\text{Cu K}_\alpha$  radiation ( $\lambda = 0.15418$  nm) at a scanning rate of  $0.02^\circ/\text{min}$ . Fourier transform infrared (FT-IR) spectra of samples were recorded on a Bio-Rad FTS135 spectrometer in the range  $500\text{--}4000\text{ cm}^{-1}$  using a KBr wafer technique, to study the formation and ripening mechanism of the samples.

### Up-flow fixed-bed adsorption experiments

The adsorption and regeneration performance of the  $\text{Fe}_3\text{O}_4$ @yeast composites was investigated in up-flow fixed-bed columns made from glass (12 cm high, 0.8 cm internal diameter) operated in continuous flow. A stock solution of MB (1000 mg/L) was prepared and further diluted to the required feed concentration in each experiment. The effect of the influent concentration (100, 150 and 200 mg/L), flow rate (5, 10, and 15 mL/min), bed depth (1.2, 2.4 and 3.6 cm, corresponding to 0.1, 0.2 and 0.3 g of adsorbent) and pH (3, 5, 7, 9, 11) on the removal of MB in the columns was investigated. The pH of the dye solutions was adjusted by adding NaOH and  $\text{H}_2\text{SO}_4$ . Samples collected from the inlet/outlet of the columns at regular intervals were analyzed using a Jenway 6405 UV–vis spectrophotometer at 664 nm. All of the experiments were performed in triplicate and at room temperature.

### Regeneration experiment

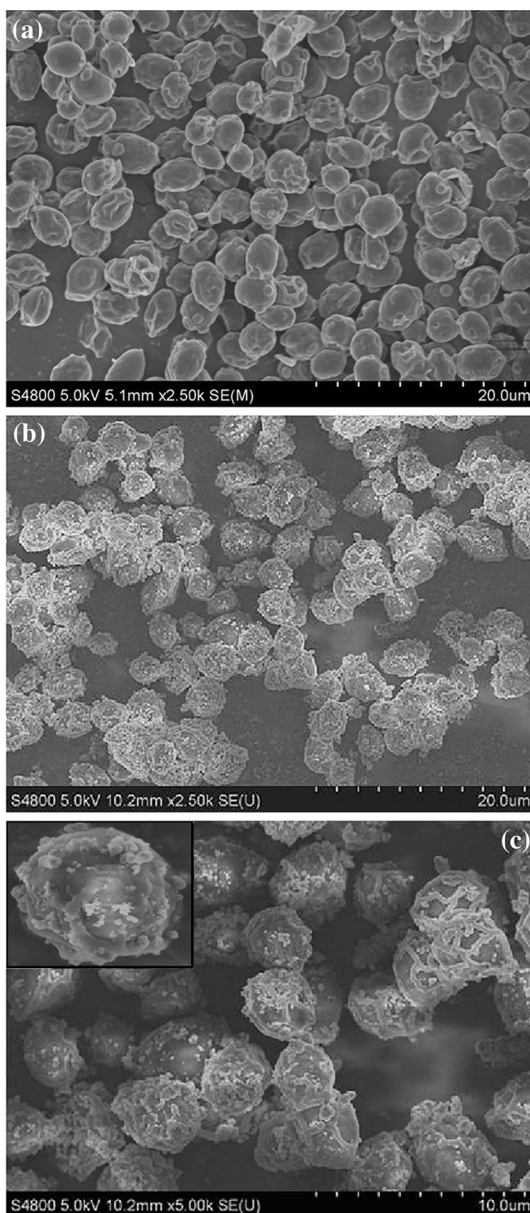
After each adsorption cycle, the exhausted column bed was rinsed by flowing 100 mL double deionized water in the upward direction at the same flow rate used during the adsorption cycle. Then the in situ regeneration of the  $\text{Fe}_3\text{O}_4$ @yeast bed was triggered by flowing a 10 %  $\text{H}_2\text{O}_2$  aqueous solution through the column bed in the upward direction at a flow rate of 1 mL/min for 1 h. The column was finally rinsed with double deionized water to remove the residual  $\text{H}_2\text{O}_2$ . After the completion of regeneration procedure, the bed was reused for the next adsorption-regeneration cycle, up to three consecutive cycles.

## Results and discussion

### Characterization and mechanism

Fig. 1 shows typical FE-SEM images of the original yeast and the as-obtained  $\text{Fe}_3\text{O}_4$ @yeast composite microspheres under different magnifications. The original

**Fig. 1** FE-SEM images of **a** the original yeast, **b** and **c**  $\text{Fe}_3\text{O}_4$ @yeast microspheres observed under different magnifications



yeast (Fig. 1a) shows cells with a smooth surface and ellipsoidal shape with regular diameter (length  $4.0 \pm 0.2 \mu\text{m}$ ; width  $2.6 \pm 0.2 \mu\text{m}$ ). The  $\text{Fe}_3\text{O}_4$ @yeast composite microspheres (Fig. 1b) maintained the ellipsoidal shape of the original yeast with the rough surface morphology and relatively good monodispersity. The dimensions of the composite microspheres slightly increased (length  $4.5 \pm 0.2 \mu\text{m}$ ; width  $3.0 \pm 0.2 \mu\text{m}$ ) suggesting that the  $\text{Fe}_3\text{O}_4$  nanoparticles (on average 20 nm, inset in Fig. 1c) were successfully attached onto the surface of yeast. The higher magnification image (Fig. 1c), shows a rough surface decorated with numerous  $\text{Fe}_3\text{O}_4$  nanoparticles with exposed yeast bare areas. Furthermore, each of the composite microspheres approached a distinct raspberry-like morphology.

The EDS analysis of the composite microspheres is shown in Fig. S1 of the Supplementary Information (SI). The C and in part the O peaks resulted from the original yeast cell wall, the Fe and part of the O originated from the  $\text{Fe}_3\text{O}_4$  supported nanoparticles, and Pt arose from the metal spraying before SEM studies. No other elements were detected, indicating that the final product was impurities free.

Fig. 2 shows the XRD patterns of the original yeast, pure  $\text{Fe}_3\text{O}_4$  nanoparticles and the  $\text{Fe}_3\text{O}_4$ @yeast composite microspheres. The amorphous yeast showed only a broad peak at around  $2\theta = 20^\circ$  (Fig. 2a). The strong and sharp diffraction peaks at  $18.4^\circ$ ,  $30.3^\circ$ ,  $35.6^\circ$ ,  $37.3^\circ$ ,  $43.2^\circ$ ,  $53.4^\circ$ ,  $57.2^\circ$  and  $62.9^\circ$  in the patterns of the  $\text{Fe}_3\text{O}_4$  nanoparticles (Fig. 2b) were indexed as (110), (220), (311), (222), (400), (422), (511) and (440) of the face center-cubic phase of  $\text{Fe}_3\text{O}_4$  (JCPDS card No. 19-0629), which agree with the literature data [22, 23]. The broad peak at  $2\theta = 20^\circ$  of the  $\text{Fe}_3\text{O}_4$ @yeast composite microspheres (Fig. 2c) originated mainly by the amorphous structure of yeast. The remaining peaks supported the incorporation of the  $\text{Fe}_3\text{O}_4$  nanoparticles in the composite and no other diffraction peaks were found in the range investigated indicating the high purity of the products. The intensity of the  $\text{Fe}_3\text{O}_4$  peaks in the

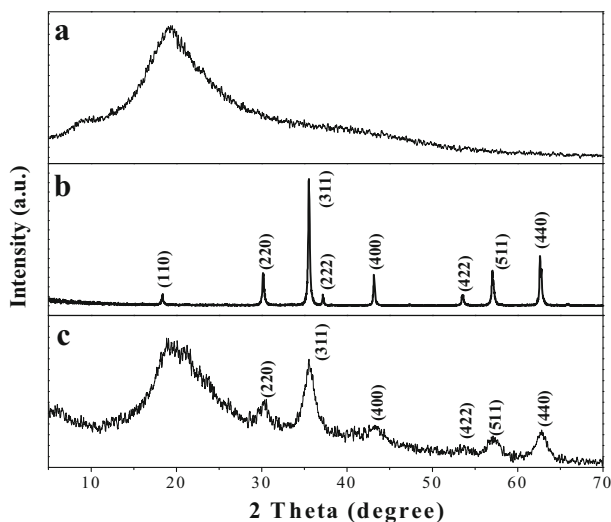


**Fig. 2** XRD patterns of **a** the original yeast, **b**  $\text{Fe}_3\text{O}_4$  nanoparticles, and **c**  $\text{Fe}_3\text{O}_4$ @yeast composite microspheres

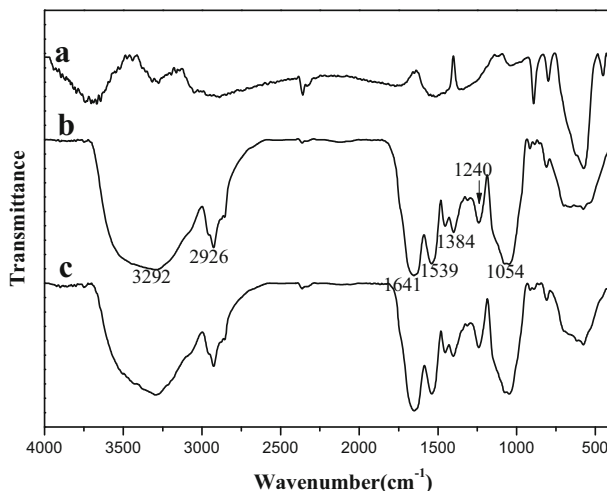


**Fig. 3** FT-IR spectrum of **a** the Fe<sub>3</sub>O<sub>4</sub> NPs, **b** the pristine of yeast and **c** Fe<sub>3</sub>O<sub>4</sub>@yeast composite microspheres

microspheres were lower than those of the pure Fe<sub>3</sub>O<sub>4</sub> nanoparticles, which may result from the smaller number of Fe<sub>3</sub>O<sub>4</sub> nanoparticles supported on the yeast surface [24, 25] and their good monodispersion surface traits [26, 27].

The ferromagnetic properties of the Fe<sub>3</sub>O<sub>4</sub>@yeast composite microspheres in aqueous solution are shown in Fig. S2 (SI). The Fe<sub>3</sub>O<sub>4</sub>@yeast composite microspheres (40 g/L) were dispersed in deionized water in a cuvette forming a stable suspension (Fig. S2a). Under the influence of a magnetic field, there was a rapid separation of the Fe<sub>3</sub>O<sub>4</sub>@yeast composite particles to the wall of the cuvette, which yielded an almost colorless aqueous solution (Fig. S2b) (SI). This indicated that the Fe<sub>3</sub>O<sub>4</sub> nanoparticles were successfully incorporated onto the surface of the yeast hosts endowing the yeast cells with magnetic properties allowing easy separation, recovery and reuse. The black color imparted by the Fe<sub>3</sub>O<sub>4</sub> nanoparticles to the ivory yeast in the composite further supports the successful incorporation of Fe<sub>3</sub>O<sub>4</sub> nanoparticles on the yeast surface.

The bonding forces acting between the nanoparticles and the yeast were investigated by FT-IR (Fig. 3). The broad and intense peaks in the region from 550 to 650 cm<sup>-1</sup> of the Fe<sub>3</sub>O<sub>4</sub> nanoparticles (Fig. 3a) are assigned to the Fe–O band. The peaks at around 3300–3700 cm<sup>-1</sup> and 1384 cm<sup>-1</sup> belong to OH stretching vibrations and to the H–O–H bending band, suggesting that H<sub>2</sub>O molecules adsorbed on the surface of Fe<sub>3</sub>O<sub>4</sub> [28]. The additional broad peaks at 3340, 1461, 1360, 1074 and 894 cm<sup>-1</sup> may result from residual hydrazine hydrate remaining from the synthesis process. Regarding the yeast (Fig. 3b), the broad and intense peaks at 3292, 2926, 1641, 1384 and 1074 cm<sup>-1</sup> are assigned to the N–H stretching and bending vibration, the CH<sub>2</sub> asymmetric and symmetric stretching vibration, the amide group, C=O stretching vibration, and the P=O stretching vibration [29–31]. In the Fe<sub>3</sub>O<sub>4</sub>@yeast spectra (Fig. 3c), except for the characteristic absorption peak of yeast, a peak appeared in the range of 550–650 cm<sup>-1</sup>. Moreover, the characteristic

peaks of yeast at 3292, 1641 and 1054  $\text{cm}^{-1}$  shifted to 3310, 1656, and 1064  $\text{cm}^{-1}$  in the  $\text{Fe}_3\text{O}_4$ @yeast composite microspheres, suggesting that the amino ( $-\text{NH}_2$ ), carboxyl ( $-\text{COO}^-$ ) and phosphate ( $-\text{OPO}_3^{2-}$ ) groups played important roles in the anchoring of the  $\text{Fe}_3\text{O}_4$  nanoparticles to the yeast surface.

Based on the above analysis, we propose a formation mechanism of  $\text{Fe}_3\text{O}_4$ @yeast composite microspheres (Fig S4a in SI). After the synthesis of  $\text{Fe}_3\text{O}_4$  nanoparticles by the hydrothermal route, the attachments of the nanoparticles onto the surface of yeast is driven by the electrostatic-interaction, self-assembly heterocoagulation between yeast cores and satellite  $\text{Fe}_3\text{O}_4$  nanoparticles. Specifically, at the synthesis pH of 5, the  $\text{Fe}_3\text{O}_4$  nanoparticles are positively charged ( $\text{pH}_{\text{iep}}$  6.5, [32]) and the yeast is negatively charged ( $\text{pH}_{\text{iep}}$  3.0, [33]). Therefore, the opposite zeta potentials of  $\text{Fe}_3\text{O}_4$  nanoparticles and yeast in the range of pH 3.0–6.5 provides a window to assemble them together. The inherent functional groups in the yeast cell wall, including phosphomannan, mannan, glucan, proteins and dextran play a significant role in the fabrication of the raspberry-like structure of the composite, since the abundant hydrophilic anion groups including  $-\text{NH}^-$ ,  $-\text{COO}^-$ , and  $-\text{OPO}_3^{2-}$  [34, 35] can accumulate more negative charges on the surface of the yeast [36]. Hereby, the positively charged  $\text{Fe}_3\text{O}_4$  nanoparticles can spontaneously attach with the negatively charged yeast, and gradually embed onto the external surface of the yeast, eventually forming the  $\text{Fe}_3\text{O}_4$ @yeast composite microspheres with a raspberry-like structure.

### Fixed-bed column studies

The partially uncovered yeast surface of the raspberry-like  $\text{Fe}_3\text{O}_4$ @yeast microspheres drives the adsorption of water contaminants. The yeast surface is usually negatively charged ( $\text{pH}_{\text{iep}}$  3.3). As a consequence, positively charged water contaminants such as cationic dyes are readily sorbed. To demonstrate this effect, the sorption of MB from aqueous solution was investigated in a continuous, up-flow, fixed-bed adsorption/regeneration system. The breakthrough curves were defined by the ratio of effluent and influent MB concentrations ( $C_t/C_0$ ) versus time ( $t$ ). The breakthrough time ( $t_b$ , time to reach 1 mg/L MB in the effluent) and the bed exhaustion time or saturation time ( $t_e$ , time to reach 99 % of the influent concentration in the effluent) were used to monitor the bed performance. To analyze the continuous flow, adsorption data included the evaluation of (a) the effluent volume  $V_{\text{eff}}$  (mL) (Eq. 1); (b) the total loading of MB to the column  $q_{\text{tot}}$  (mg) (Eq. 2) at a given flow rate and influent concentration; (c) the total amount of MB fed to the column  $m_{\text{tot}}$  (mg) (Eq. 3); (d) the total percentage removal efficiency  $\varphi$  of MB (Eq. 4); and (e) the equilibrium column loading  $q_e$  (mg/g) (Eq. 5).

$$V_{\text{eff}} = F \cdot t_e \quad (1)$$

$$q_{\text{tot}} = \frac{FA}{1000} = \frac{F}{1000} \int_{t=0}^{t=t_{\text{tot}}} C_{\text{ad}} dt \quad (2)$$



$$m_{tot} = \frac{C_0 F t_{tot}}{1000} \quad (3)$$

$$\phi\% = \frac{q_{tot}}{m_{tot}} \times 100 \quad (4)$$

$$q_e = \frac{q_{tot}}{m} \quad (5)$$

where  $F$  is the volumetric flow rate (mL/min),  $A$  is the area under the breakthrough curve,  $C_{ads}$  (mg/L) is the adsorbed MB concentration and  $m$  is the amount of  $Fe_3O_4@yeast$  in the fixed bed (g).

### *Influence of influent dye concentration, flow rate, bed height and mass transfer*

The breakthrough curves of MB for an influent dye concentration varying from 100 to 200 mg/L are shown in Fig. 4a. In these experiments, the flow rate, bed height, and pH were kept constant at 5 mL/min, 1.2 cm and 7, in order. The adsorption data and the parameters are also presented in Table 1. The observed breakthrough curves

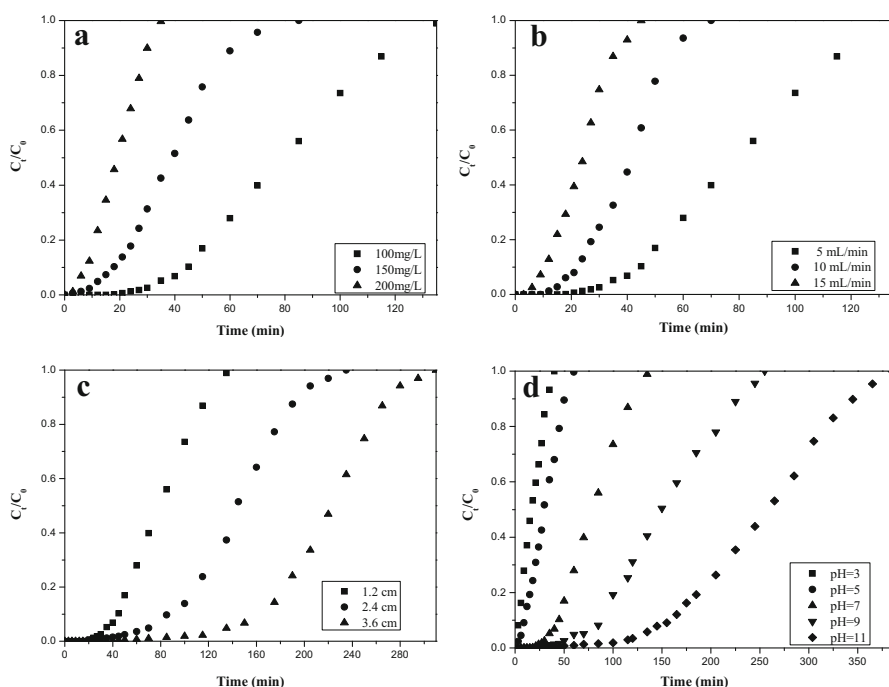


**Fig. 4** The breakthrough curves for MB adsorption by  $Fe_3O_4@yeast$  composites **a** at different influent dye concentration (flow rate = 5 mL/min, bed height = 1.2 cm, and pH 7.0), **b** at different flow rate (influent dye concentration = 100 mg/L, bed height = 1.2 cm, and pH 7.0), **c** at different bed height (influent dye concentration = 100 mg/L, flow rate = 5 mL/min, and pH 7.0) and **d** at different pH (influent dye concentration = 100 mg/L, flow rate = 5 mL/min, and bed height = 1.2 cm)

**Table 1** Column data and parameters obtained at different conditions

Process parameters	$t_b$ (min)	$t_e$ (min)	$V_{eff}$ (mL)	$q_{tot}$ (mg)	$m_{tot}$ (mg)	Dye removal $\varphi$ %	$q_e$ (mg/g)
Initial dye concentration, $C_0$ (mg/L) ( $F = 5$ mL/min, $Z = 1.2$ cm, pH 7.0)							
100	24	135	675	40.1	67.5	59.3	400.5
150	6	70	350	29.4	52.5	56.0	294.0
200	3	35	175	19.1	35.0	54.6	191.1
Flow rate, $F$ (mL/min) ( $C_0 = 100$ mg/L, $Z = 1.2$ cm, pH 7.0)							
5	24	135	675	40.1	67.5	59.3	400.5
10	18	85	650	35.5	65.0	54.6	355.0
15	9	35	630	31.1	63.0	49.3	310.9
Bed height, $Z$ (cm) ( $C_0 = 100$ mg/L, $F = 5$ mL/min, pH 7.0)							
1.2	24	135	675	40.1	67.5	59.3	400.5
2.4	85	235	1175	74.2	117.5	63.1	370.8
3.6	150	310	1550	108.8	155.0	70.2	362.8
pH ( $C_0 = 100$ mg/L, $F = 5$ mL/min, $Z = 1.2$ cm)							
3	6	40	200	9.9	20.0	49.5	99.0
5	12	60	300	15.2	30.0	50.5	151.5
7	24	135	675	40.0	67.5	59.3	400.5
9	35	255	1275	78.0	127.5	61.2	780.1
11	70	385	1925	122.1	192.5	63.4	1221.0

followed the typical S-shaped profile. However, a near linear profile was observed when the influent MB concentration increased to 200 mg/L. The breakthrough and exhaustion times decreased with increasing influent dye concentration due to the faster rate of sorbent saturation. When  $C_0$  increased from 100 to 200 mg/L, the equilibrium column loading ( $q_e$ ) decreased from 400.5 to 191.1 mg/g (Table 1), which suggests mass transfer limitations. Consequently, the bed exhaustion is reached before the complete saturation of the adsorbent. Simultaneously, the percent removal of MB for the tested influent concentrations decreased from 59.3 to 54.6 %.

The effect of flow rate (Fig. 4b; Table 1) was examined by varying it from 5 to 15 mL/min while  $C_0$ , bed height and pH were kept constant at 100 mg/L, 1.2 cm, and 7, in order. The breakthrough curves became steeper and shifted towards shorter times as the flow rate increased, while the breakthrough time and the exhaustion time decreased from 24 to 9 min and from 135 to 35 min, respectively. Furthermore,  $q_e$  and  $\varphi$  decreased as the flow rate increased, suggesting a slow intraparticle adsorption kinetics compared with the column saturation dynamics. Lower flow rates and longer residence time of MB results in a more efficient diffusion process through the sorbent and therefore a higher equilibrium column loading.

The effect of bed height on MB removal (Fig. 4c; Table 1) was investigated at constant flow rate of 5 mL/min and 100 mg/L influent dye concentration. An increase of the breakthrough time, exhaustion time and percentage removal, was observed, when the bed height rose from 1.2 to 3.6 cm (loading of 0.1–0.3 g of

Fe<sub>3</sub>O<sub>4</sub>@yeast) which results from the larger sorbent total mass. The significant reduction in the loading capacity observed with bed height was ascribed to an increase of pressure drop through the bed, which progressively decreases the rate of intraparticle diffusion.

The equilibrium sorption capacity of the Fe<sub>3</sub>O<sub>4</sub>@yeast composite microspheres from batch recirculation experiments at  $C_0$  equal to 100 mg/L and pH 7 was 403.2 mg/g, which suggest that MB mass transfer was negligible only at  $C_0 = 100$  mg/L,  $Z = 1.2$  cm and pH 7 (Table 1).

### *Influence of pH*

In these experiments, the pH of MB solution fed to the bed was fixed at 3, 5, 7, 9, and 11, while  $C_0$ , flow rate and bed height were kept constant at 100 mg/L, 5 mL/min, and 1.2 cm. The results (Fig. 4d; Table 1) show that the adsorption capacity and dye removal rate increased with an increase of pH. Bed exhaustion occurred at 35, 60, 135, 255 and 355 min for pH of 3.0, 5.0, 7.0, 9.0 and 11.0. This phenomenon is governed by the electrostatic interaction between the dye and the surface charge of the adsorbent [37]. The adsorption of cationic dyes is favored at  $\text{pH} > \text{pH}_{\text{iep}}$  ( $\text{pH}_{\text{iep}}$  = isoelectric point, e.g. on  $\text{COO}^-$  groups) and anionic dyes at  $\text{pH} < \text{pH}_{\text{iep}}$  (e.g. on Lewis-base-type basal plane sites) [38]. MB is a cationic dye, which exists in solution in the form of positively charged ions. The surface properties of the yeast cores ( $\text{pH}_{\text{iep}}$  3.3) and Fe<sub>3</sub>O<sub>4</sub> nanoparticles ( $\text{pH}_{\text{iep}}$  6.8) are also affected by pH. At pH 3, the surface charge of both yeast and Fe<sub>3</sub>O<sub>4</sub> is positive, and thus the abundance of  $\text{H}^+$  compete with the cationic MB molecules, reducing the adsorption capacity of the bed causing a rapid breakthrough. At pH 5, the yeast surface has negative and the Fe<sub>3</sub>O<sub>4</sub> nanoparticles have positive charge, which increases the adsorption of MB through the surface of the yeast resulting in a longer breakthrough time. At pH 7, 9 and 11, both yeast and Fe<sub>3</sub>O<sub>4</sub> have negative charges and the adsorption performance of the bed increases very rapidly has the pH increases. The maximum equilibrium column capacity (1221 mg/g) and MB removal efficiency (63.4 %) appear at pH 11, as also reported in other studies with other sorbents [39].

### **Mathematical modeling of breakthrough curves**

Thomas [40] and Yoon-Nelson [41] models were used to model the experimental breakthrough curves at different influent dye concentration, flow rate, bed height and pH. The linearized form of the Thomas model is widely used to describe column breakthrough data:

$$\ln\left(\frac{C_0}{C_t} - 1\right) = \frac{k_{\text{Th}}q_0m}{F} - k_{\text{Th}}C_0t \quad (6)$$

with  $C_0$  and  $C_t$  the influent and effluent dye concentrations (mg/L),  $k_{\text{Th}}$  the Thomas rate constant (mL/min mg),  $q_0$  the equilibrium adsorption capacity (mg/g),  $m$  the mass of the adsorbent (g), and  $F$  the solution flow rate (mL/min). The plots of

**Table 2** Parameters predicted from the Thomas and Yoon-Nelson models

Parameters	Thomas model			Yoon-Nelson model		
	$k_{Th}$ (mL/min-mg)	$q_0$ (mg/g)	$R^2$	$k_{YN} \times 10^{-3}$ (min <sup>-1</sup> )	$\tau$ (min)	$R^2$
Initial dye concentration (mg/L)						
100	7.29	396.3	0.97	72.9	79.2	0.97
150	8.68	254.2	0.98	130.2	33.9	0.98
200	12.49	153.8	0.90	249.7	15.3	0.90
Flow rate (mL/min)						
5	7.29	396.3	0.97	72.9	79.2	0.97
10	13.44	382.4	0.98	134.4	38.2	0.98
15	17.36	359.9	0.98	173.6	23.9	0.98
Bed height (cm)						
1.2	7.29	396.3	0.97	72.9	79.2	0.97
2.4	4.10	365.4	0.99	49.2	131.7	0.99
3.6	3.38	357.5	0.98	33.8	214.5	0.98
pH						
3	14.01	88.2	0.97	140.1	17.6	0.97
5	11.10	152.8	0.96	111.0	30.5	0.96
7	7.29	396.3	0.97	72.9	79.2	0.97
9	3.86	754.5	0.98	38.6	150.8	0.98
11	2.42	1265.3	0.99	24.2	253.1	0.99

$\ln[(C_0/C_t)-1]$  versus time ( $t$ ) give a straight line of slope ( $-k_{Th}C_0$ ) and intercept ( $k_{Th}q_m m/F$ ) (figure not shown).

The linearized form of the Yoon-Nelson model is:

$$\ln\left(\frac{C_t}{C_0 - C_t}\right) = k_{YN}t - k_{YN}\tau \quad (7)$$

with the adsorption capacity in the Yoon-Nelson model calculated from [42]:

$$q_{YN} = \frac{q_{tot}}{m} = \frac{C_0 F \tau}{1000m} \quad (8)$$

with,  $k_{YN}$  the Yoon-Nelson rate constant (min<sup>-1</sup>),  $\tau$  the time required for reaching 50 % adsorbate breakthrough (min) and other parameters as above. The parameters  $k_{YN}$  and  $\tau$  are determined from the slope and intercept of the linear plots of  $\ln[C_t/(C_0 - C_t)]$  versus time ( $t$ ).

Table 2 summarizes the model parameters determined from fitting the Thomas and Yoon-Nelson models to the experimental data. The rate constant ( $k_{Th}$ ) in Table 2, which characterizes the rate of solute transfer from the solution to the surface of solid, increased with increasing influent dye concentration and flow rate and decreased with bed height and pH. These results support an increase of the importance of mass transfer limitations in the fixed bed as flow rate and dye concentration decreases and bed height and pH increases. The bed capacity  $q_0$

calculated from the Thomas model decreased as the dye concentration, flow rate and bed height increased, because of intraparticle diffusion resistance. The values of  $k_{YN}$  increased with an increase in the influent dye concentration and flow rate, while the corresponding  $\tau$  values followed an opposite trend. Moreover, the values of  $k_{YN}$  decreased with an increase in both bed height and pH, whereas, a reverse trend was observed for the values of  $\tau$ .

The theoretical column adsorption capacities calculated from the Thomas and Yoon-Nelson models were compared to the experimental results (Fig. S3a in SI). Here, it was observed that the theoretical column capacity predicted by the Yoon-Nelson model was closer to the experimental data. In addition, the experimental  $\tau$  values and the theoretical  $\tau$  values from Yoon-Nelson model were in close agreement (Fig. S3b in SI). The Thomas model neglects external mass transfer and internal diffusion and assumes second-order reversible adsorption kinetics without axial dispersion. Therefore, the Thomas model provided a closer fit only for the condition in which mass transfer could be considered negligible (Fig. S3a in SI and Table 1). In contrast, the Yoon–Nelson model is based on the assumption that the rate of decrease in the probability of biosorption for each adsorbate molecule is proportional to the probability of adsorbate adsorption and the probability of adsorbate breakthrough on the biosorbent. The parameters in this model are adjustable and can fit experimental data that may have also been affected by external mass transfer resistances, internal diffusion and axial dispersion. Consequently, the Yoon–Nelson model provided a closer fit of the experimental data within the range of experimental conditions.

### Contaminant oxidation and sorbent regeneration

The magnetic property imparted by the supported  $\text{Fe}_3\text{O}_4$  on the yeast host is an important functionality. However, a more important functionality is the ability of  $\text{Fe}_3\text{O}_4$  to trigger the heterogeneous Fenton oxidation reaction, which oxidizes the adsorbed contaminants regenerating the sorbent. The performance of the fixed-bed was evaluated for three consecutive adsorption/regeneration cycles. The influent MB concentration, flow rate, bed height and pH were fixed at 100 mg/L, 5 mL/min, 1.2 cm and 7.

The column capacity decreased after each regeneration cycle although MB uptake and removal rate remained very high (Table 3). The column bed exhibited equilibrium column loading capacities of over 273.5 mg/g dry beads and removal rate over 57.5 % in all three cycles. The reduction in column capacity should be attributed to the inability of the Fenton reaction to remove MB sorbed deeply into

**Table 3** Column data and parameters obtained after Fenton-like regeneration

Cycle time	$t_b$	$t_e$	$V_{\text{eff}}$ (mL)	$q_{\text{tot}}$ (mg)	$m_{\text{tot}}$ (mg)	Dye removal $\varphi$ %	$q_e$ (mg/g)
1th	24	135	675	40.1	67.5	59.3	400.5
2th	18	115	500	33.8	57.5	58.7	337.5
3th	12	95	300	27.4	47.5	57.6	273.5

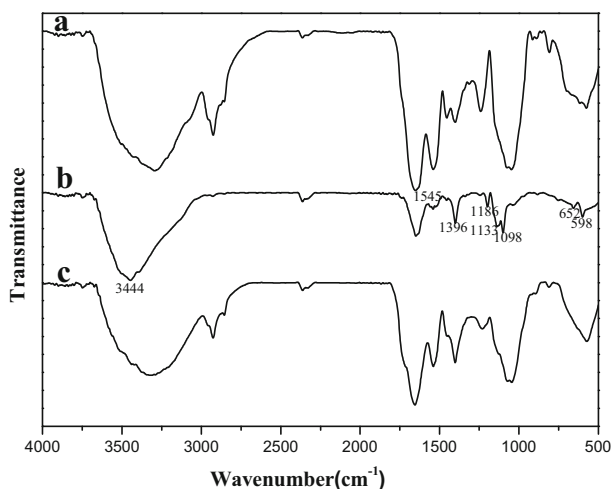


**Fig. 5** FT-IR spectra of **a**  $\text{Fe}_3\text{O}_4$ @yeast composites, **b** the  $\text{Fe}_3\text{O}_4$ @yeast composites saturated by MB and **c** the saturated composites after Fenton-like reaction

the yeast cores, since  $\text{Fe}_3\text{O}_4$  is primarily supported on the surface. Comparing the parameters  $q_e$  and  $\varphi$  % with those reported elsewhere [43, 44], the  $\text{Fe}_3\text{O}_4$ @yeast adsorbent presents the advantage that it can be easily regenerated in situ and reused in multiple cycles.

Fig. 5 shows the FT-IR spectra of (a) the synthesized  $\text{Fe}_3\text{O}_4$ @yeast composite, (b) the  $\text{Fe}_3\text{O}_4$ @yeast composite saturated by MB and (c) the saturated composites after Fenton-like reaction.

The spectra of the composite saturated with MB (trace b) displays new band peaks and some obvious red shift peaks in comparison to the fresh composite (trace a). The new bands peaks originated from the MB, particularly those at 1558, 1396, 1051, and 578  $\text{cm}^{-1}$ , which correspond to the stretching vibrations of the aromatic ring, the C–C and C–S bonds, and the frame vibration of C–S–C [45]. The red shift peaks, such as the bands at 3292, 1641 and 1054  $\text{cm}^{-1}$ , suggested the participation of  $-\text{OH}^-$ ,  $-\text{COO}^-$ , and  $-\text{OPO}_3^{2-}$  groups in the adsorption reaction [46]. Notably, the bands associated with MB disappeared after the application of the Fenton-like reaction (trace c).

A schematic of the adsorption and in situ regeneration mechanisms of the  $\text{Fe}_3\text{O}_4$ @yeast composite microspheres is presented in Fig. S4b (SI). The regeneration processes might be attributed to the synergistic effect, which works by integrating the biosorption properties of yeast with the catalytic oxidation properties of the supported  $\text{Fe}_3\text{O}_4$  nanoparticles. Specifically, the MB molecules are first removed from aqueous solution by biosorption and pre-concentrated on the bare areas of the  $\text{Fe}_3\text{O}_4$ @yeast composite microspheres. Then, the enriched MB molecules are decomposed by the  $\text{Fe}_3\text{O}_4/\text{H}_2\text{O}_2$  Fenton-like oxidation reaction. The  $\text{H}_2\text{O}_2$  introduced to the MB saturated column is catalytically decomposed by the supported  $\text{Fe}_3\text{O}_4$  nanoparticles yielding  $\cdot\text{OH}$  radicals, which then attack the adsorbed MB molecules regenerating the sorbent. The targeted localized reaction at or in the close proximity of the composite surface is

much more efficient than the same Fenton-like reaction carried out by  $\text{Fe}_3\text{O}_4$  particles in suspensions in slurry reactors. Less catalyst is used,  $\cdot\text{OH}$  scavenging reactions species in solution are minimized (e.g., carbonates and not targeted species) and also the reaction acts on a much higher pollutant load, which increases the contaminant removal rate (i.e., first order contaminant removal). In return, the regenerated surfaces of the yeast core can provide continuous adsorption sites for the biosorption of contaminants in repeated cycles.

## Conclusion

In this study, we have investigated a new composite material, which integrates the biosorption features of yeast cells with the magnetic and catalytic properties of  $\text{Fe}_3\text{O}_4$  nanoparticles, for the effective removal and oxidative destruction of contaminants in water and wastewater. The raspberry-like  $\text{Fe}_3\text{O}_4$ @yeast composite microspheres, were fabricated via a simple electrostatic self-assembly approach using inexpensive and abundant raw materials. These composites exhibited a ferromagnetic property that allows them to be easily separated/recovered by use of an external magnetic field. The adsorption and regeneration performance by a Fenton-like reaction of the microspheres was investigated for the continuous removal of the cationic dye methylene blue in an up-flow packed column. The adsorption process was controlled by the electrostatic interactions between the adsorbent and the contaminant. The adsorbent is suitable for the adsorption of positively charged compounds at mildly acidic pH, neutral and alkaline pH, with the highest performance observed at alkaline pH. The raspberry-like  $\text{Fe}_3\text{O}_4$ @yeast composite material can be easily regenerated by applying a Fenton-like reaction and reused. Considering the facile method of fabrication of the composite from abundant and inexpensive raw materials, the easy recovery and separation in water, the superior adsorption performance, the simple and effective way of regeneration and the robustness of the adsorbent for consecutive adsorption/regeneration cycles, we conclude that the raspberry-like  $\text{Fe}_3\text{O}_4$ @yeast magnetic microsphere should be a promising and practical adsorbent for the removal and destruction of positively charged organic compounds in wastewater. The embedding of  $\text{Fe}_3\text{O}_4$  onto the yeast surface can be extended to the simple fabrication of other  $\text{Fe}_3\text{O}_4$  nanoparticles/bio-macromolecules or other magnetic oxides/yeast materials with similar structure.

**Acknowledgments** This work was supported by China Postdoctoral Science Special Foundation, Scientific Research Foundation for the Returned Overseas Chinese Scholars, National Natural Science Foundation of China (No.21176031) and Fundamental Research Funds for the Central Universities (No. 2013G2291015).

## References

1. Wu RC, Qu JH (2004) *Water Environ Res* 76:2637–2642
2. Kovacic P, Somanathan R (2014) *J Appl Toxicol* 34:825–834
3. Drogui P, Blais JF (2007) *Recent Pat Eng* 1:257–272
4. Solís M, Solís A, Pérez HI, Manjarrez N, Flores M (2012) *Process Biochem* 47:1723–1748

5. Janaki V, Vijayaraghavan K, Ramasamy AK, Lee KJ, Oh BT, Kamala-Kannan S (2012) *J Hazard Mater* 241–242:110–117
6. Chen AH, Chen SM (2009) *J Hazard Mater* 172:1111–1121
7. Yu JX, Chi RA, Su XZ, He ZY, Qi YF, Zhang YF (2010) *J Hazard Mater* 177:222–227
8. Rache ML, García AR, Zea HR, Silva AMT, Madeira LM, Ramírez JH (2014) *Appl. Catal. B: Environ.* 146:192–200
9. Gu L, Huang S, Zhu N, Zhang D, Yuan H, Lou Z (2013) *J Hazard Mater* 263:450–457
10. Maria ADL, Marta S, Juan B (2013) *Reac Kinet Mech Cat* 110:101–117
11. Liang X, Zhong Y, Zhu S, Zhu J, Yuan P, He H, Zhang J (2010) *J Hazard Mater* 181:112–120
12. Xavier S, Gandhimathi R, Nidheesh PV, Ramesh ST (2013) *Desalin Water Treat* 53(1):109–118. doi:[10.1080/19443994.2013.844083](https://doi.org/10.1080/19443994.2013.844083)
13. Wu RC, Qu JH (2004) *Water Environ Res* 76:2637–2642
14. Kong SH, Watts RJ, Choi JH (1998) *Chemosphere* 37:1473–1482
15. Tyre BW, Watts RJ, Miller GC (1991) *J Environ Qual* 20:832–838
16. Guo SJ, Dong SJ, Wang EK (2009) *J Phys Chem C* 113:5485–5492
17. Zhang L, Li Y, Sun JQ, Shen JC (2008) *Langmuir* 24:10851–10857
18. Liu HL, Wang D, Yang XL (2012) *Colloids Surf A* 397:48–58
19. Wang X, Akagi T, Akashi M, Masanori B (2007) *Mini-Rev Org Chem* 4:51–59
20. Tsai HJ, Lee YL (2007) *Langmuir* 23:12687–12692
21. Bai B, Quici N, Li ZY, Puma GL (2011) *Chem Eng J* 170:451–456
22. Zhang SX, Zhao XL, Niu HY, Shi YL, Cai YQ, Jiang GB (2009) *J Hazard Mater* 167:560–566
23. Zhu T, Chen JS, Lou XW (2011) *David. J Phys Chem C* 115:9814–9820
24. Duan LF, Jia SS, Wang YJ, Chen J, Zhao LJ (2009) *J Mater Sci* 44:4407–4412
25. Kim NS, Kim JD (2012) *J Ind Eng Chem* 18:1721–1729
26. Su XD, Zhao JZ, Li YL, Zhu YC, Ma XK, Sun F, Wang ZC (2009) *Colloids Surf A* 349:151–155
27. Hassan MS, Amna T, Yang OB, Kim HC, Khil MS (2012) *Ceram Int* 38:5925–5930
28. Li ZP, Gao L, Zheng S (2002) *Appl Catal A* 236:163–171
29. Kumar S, Surendar T, Kumar B, Baruah A, Shanker V (2013) *J Phys Chem C* 117:26135–26143
30. Cui JJ, He W, Liu HT, Liao SJ, Yue YZ (2009) *Colloids Surf B* 74:274–278
31. Blakeslee KC, Robert A, Condrate SR (1971) *J Am Ceram Soc* 54:559–563
32. Joris SJ, Amberg CH (1971) *J Phys Chem* 75:3172–3178
33. Chang YC, Chen DH (2005) *J. Colloid Interf Sci* 283:446–451
34. Mercier-Bonin M, Ouazzani K, Schmitz P, Lorthois S (2004) *J Colloid Interf Sci* 271:342–350
35. Wang JL, Chen C (2009) *Biotechnol Adv* 27:195–226
36. Mann S, Archibald DD, Didymus JM, Douglas T, Heywood BR, Meldrum FC, Reeves NJ (1993) *Science* 261:1286–1292
37. Ai LH, Huang HY, Chen ZL, Wei X, Jiang J (2010) *Chem Eng J* 156:243–249
38. Salleh MAM, Mahmoud DK, Karim WAWA, Idris A (2011) *Desalination* 280:1–13
39. Doğan M, Alkan M (2003) *Chemosphere* 50:517–528
40. Thomas HC (1944) *J Am Chem Soc* 66:1664–1666
41. Yoon YH, Nelson JH (1984) *Am Ind Hyg Assoc J* 45:509–516
42. Hasan SH, Ranjan D, Talat M (2010) *J Hazard Mater* 181:1134–1142
43. Kavitha D, Namasivayam C (2007) *Bioresour Technol* 98:14–21
44. Chen L, Bai B (2013) *Ind Eng Chem Res* 52:15568–15577
45. Ai LH, Zhang CY, Liao F, Wang Y, Li M, Meng LY, Jiang J (2011) *J Hazard Mater* 198:282–290
46. Mohan SV, Mohan SK, Kathikeyan MJ (2001) *J Sci Ind Res* 60:410–415